Experimental implementation of quantum gates through actuator qubits

Jingfu Zhang,[1] Daniel Burgarth,[2] Raymond Laflamme,[3,4] and Dieter Suter[1]
[1]*Fakultät Physik, Technische Universität Dortmund, D-44221 Dortmund, Germany*
[2]*Institute of Mathematics, Physics and Computer Science, Aberystwyth University, Aberystwyth SY23 3BZ, United Kingdom*
[3]*Institute for Quantum Computing and Department of Physics, University of Waterloo, Waterloo, Ontario, Canada N2L 3G1*
[4]*Perimeter Institute for Theoretical Physics, Waterloo, Ontario, N2J 2W9, Canada*
(Received 27 May 2014; revised manuscript received 9 December 2014; published 22 January 2015)

Universal quantum computation requires the implementation of arbitrary control operations on the quantum register. In most cases, this is achieved by external control fields acting selectively on each qubit to drive single-qubit operations. In combination with a drift Hamiltonian containing interactions between the qubits, this allows the implementation of arbitrary gate operations. Here, we demonstrate an alternative scheme that does not require local control for all qubits: we implement one- and two-qubit gate operations on a set of target qubits indirectly, through a combination of gates on directly controlled actuator qubits with a drift Hamiltonian that couples actuator and target qubits. Experiments are performed on nuclear spins, using radio-frequency pulses as gate operations and magnetic-dipole couplings for the drift Hamiltonian.

DOI: 10.1103/PhysRevA.91.012330 PACS number(s): 03.67.Lx, 03.67.Pp, 76.60.−k

I. INTRODUCTION

Techniques for controlling quantum systems [1–3] have been developed in various fields including quantum computing, where quantum mechanical two-level systems (qubits) are used to store information and external control fields process the information by driving quantum gate operations [4–6]. A general purpose quantum computer requires that the control operations can implement all possible logical operations. This can be achieved, e.g., by generating arbitrary rotations of all qubits and a static system Hamiltonian that includes interactions between pairs of qubits [5,6].

In some cases, this approach is difficult or impossible to implement. Examples include systems, where some qubits couple weakly or not at all to external fields, e.g., when qubits are stored in noiseless or decoherence-free subspaces [7] or in the case of hybrid quantum registers consisting of electronic and nuclear spins [8–10]. While qubits in noiseless subsystems do not interact with control fields by design, the interaction of nuclear spins with control fields is some four orders of magnitude weaker than that of electronic spins. Control operations generated by direct irradiation of nuclear spins are therefore slow, and it might be desired to avoid them. A number of recent papers [11–16] proposed schemes for implementing quantum control by directly manipulating only a small subset of qubits. In the following, we distinguish between the directly controlled qubits, the actuator qubits, and the indirectly controlled qubits, to which we refer as target qubits. Two similar examples were recently reported for the case of spin systems consisting of an electron spin as actuator and nuclear spins as target qubits, where the hyperfine interaction was exploited for controlling one or two nuclear spin qubits [15,16].

Obviously the type of the exploited couplings between qubits and the size of the whole system are crucial factors for the degree of controllability. This point is the main motivation for the current work. Here, we use heteronuclear spin systems, where one spin species is the actuator subsystem, while the other species represents the target subsystem, to investigate the degree of controllability of the qubits with magnetic-dipole couplings in three- and five-qubit systems. Compared to previous work, we extend the size of the total quantum register to five qubits. We first determine the dynamical Lie algebra to determine to what degree our system is controllable [17]. The algebra contains several interesting quantum gates, including an entangling gate used in previous work [16].

II. LIE ALGEBRA AND CONTROLLABILITY

We use two different systems to demonstrate the indirect control approach. All the qubits are nuclear spins, and the interactions between them are magnetic-dipole couplings. The smaller one consists of one actuator qubit and two target qubits, and the larger of three actuator qubits and two target qubits.

A. AT_2 system

In the smaller system, we denote the actuator qubit as qubit 1, and two target qubits as qubits 2 and 3. The static Hamiltonian for the whole system is

$$H = H_A + H_T + H_{AT}, \tag{1}$$

where H_A refers to the actuator system, H_T to the target system, and H_{AT} describes the interaction between them. Their structure is

$$H_A = -\pi \nu_1 Z_1, \tag{2}$$

$$H_T = -\pi(\nu_2 Z_2 + \nu_3 Z_3) + \frac{\pi D_{23}}{2}(2Z_2Z_3 - X_2X_3 - Y_2Y_3), \tag{3}$$

$$H_{AT} = \pi(D_{12}Z_1Z_2 + D_{13}Z_1Z_3). \tag{4}$$

Here X_i, Y_i, Z_i denote Pauli matrices acting on qubit i, ν_i denote the chemical shifts, and D_{ij} the dipolar coupling constants. The control fields are applied only to qubit 1, so the control Hamiltonian can be written as

$$H_C(t) = B_x(t)X_1 + B_y(t)Y_1. \tag{5}$$

The Lie algebra of the possible control operations on this system is spanned by the operators that can be generated by repeatedly evaluating the commutators between the control Hamiltonian H_C and the drift Hamiltonian H [17]. The resulting Lie algebra includes 22 terms written as

$$\begin{aligned}&\{X_1,Y_1,Z_1\}\\&\quad\otimes\{E_2E_3,Z_2,Z_3,Y_2X_3-X_2Y_3,X_2X_3+Y_2Y_3,Z_2Z_3\},\{E_1\}\\&\quad\otimes\{Y_2X_3-X_2Y_3,X_2X_3+Y_2Y_3,Z_2-Z_3,-\nu_2Z_2-\nu_3Z_3\\&\qquad+D_{23}Z_2Z_3\},\end{aligned}\tag{6}$$

where E_k is the unit operator of spin k. Clearly this allows full quantum control of the actuator system, but it does not allow full control of the whole system, which would require $4^3=64$ operators. Nevertheless, it allows the implementation of many useful control operations in the target system. The interesting terms include the Dzyaloshinskii-Moriya interaction $Y_2X_3-X_2Y_3$, which is an exchange interaction relevant for some multiferroic materials [18,19], the three-body interaction $Z_1Z_2Z_3$ [20], which is a useful resource for implementing time-optimal operations [21,22], and the XY-interaction $X_2X_3+Y_2Y_3$, which allows, e.g., the implementation of a quantum state transfer along a spin chain [23–25].

The terms in the Lie algebra (6) can be simplified by choosing specific evolution times. For example, from the last element

$$-(\nu_2Z_2+\nu_3Z_3)+D_{23}Z_2Z_3,\tag{7}$$

we can generate

$$U(t)=e^{-it[-(\nu_2Z_2+\nu_3Z_3)+D_{23}Z_2Z_3]}.\tag{8}$$

For times

$$t_m=\frac{m\pi}{D_{23}},\tag{9}$$

where m is an arbitrary integer, we obtain

$$U(t_m)=e^{it_m(\nu_2Z_2+\nu_3Z_3)}.\tag{10}$$

Since Z_2-Z_3 is in the Lie algebra, we can also implement

$$U(t)=e^{-it(\nu_2Z_2-\nu_3Z_3)}.\tag{11}$$

By combining Eqs. (10) and (11), we can obtain single-qubit z rotations as

$$U_{z,k}(\theta)=e^{i\frac{\theta}{2}Z_k}\tag{12}$$

for certain angles, where $k=2,3$.

B. A_3T_2 system

In the larger system, we denote the actuator qubits as qubits 1–3 and two target qubits as qubits 4 and 5. Compared with the three-qubit system, this system contains two additional qubits in the actuator system while the size of the target system is the same. This larger system was chosen as a first step on the way to implementing such control schemes in scalable systems, which require larger numbers of controlled qubits. As an example, the implementation of quantum error correction requires at least five physical qubits for a perfect quantum error correction code [26–28].

As in the three-qubit case, the actuator system of the five-qubit system can be fully controlled; i.e., we can implement the set of operations spanned by $\mathcal{L}_a=\{E_1,X_1,Y_1,Z_1\}\otimes\{E_2,X_2,Y_2,Z_2\}\otimes\{E_3,X_3,Y_3,Z_3\}-\{E_1E_2E_3\}$. The full set of operations that can be applied to the five-qubit system includes 382 terms represented as

$$\begin{aligned}\mathcal{L}_a\otimes&\{E_4E_5,Z_4,Z_5,Y_4X_5-X_4Y_5,X_4X_5+Y_4Y_5,Z_4Z_5\},\\&\{E_1E_2E_3\}\otimes\{Y_4X_5-X_4Y_5,X_4X_5+Y_4Y_5,Z_4-Z_5,\\&-\nu_4Z_4-\nu_5Z_5+D_{45}Z_4Z_5\}.\end{aligned}\tag{13}$$

The result is similar to that of the three-qubit system: full quantum control of the actuator system is possible, in combination with similar operators for the target system.

III. TEST SYSTEMS

For the experimental implementation, we chose the two molecules shown in Fig. 1. They were dissolved in the nematic liquid crystal solvents 1-(trans-4-hexylcyclohexyl)-4-isothiocyanatobenzene, and ZLI- 1132 for molecules (a) and (c), respectively. The measured parameters of the spins

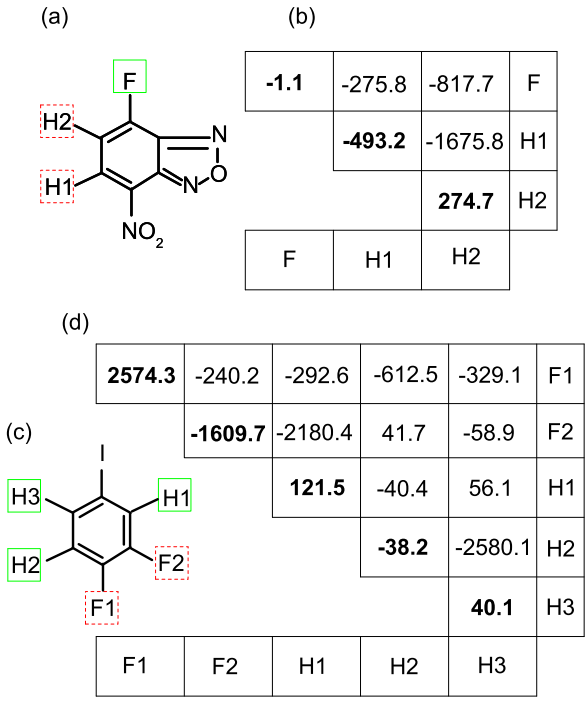

FIG. 1. (Color online) Structures and Hamiltonian constants of the molecules used as quantum registers. The actuator and target qubits are marked by solid and dashed rectangles, respectively. (a) 4-fluoro-7-nitro-2,1,3-benzoxadiazole. The fluorine spin F is used as the actuator qubit 1, and the proton spins H1 and H2 are the target qubits 2 and 3. (b) Hamiltonian parameters of molecule (a) in frequency units (Hz): the diagonal elements are the chemical shifts in a 11.7 T field, the off-diagonal terms represent the dipolar coupling constants. The liquid crystal solvent is 1-(trans-4-hexylcyclohexyl)-4-isothiocyanatobenzene. (c) 1,2-difluoro-4-iodobenzene. The proton spins H1–H3 are the actuator qubits 1–3, and the fluorine spins F1 and F2 are the target qubits 4 and 5. (d) The Hamiltonian parameters of the molecule (c). The liquid crystal solvent is ZLI- 1132.

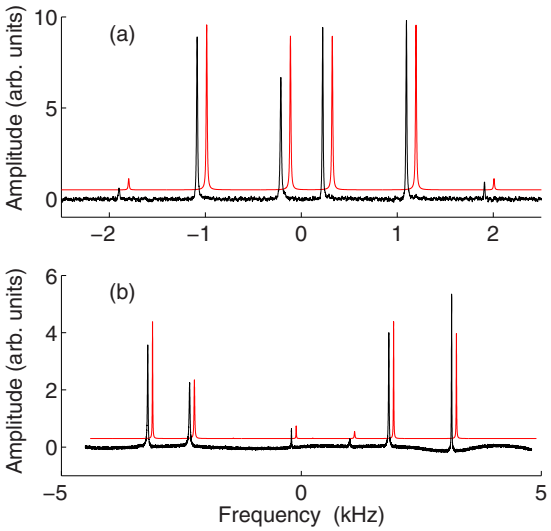

FIG. 2. (Color online) (a) ^{19}F and (b) ^{1}H -NMR spectra of 4-fluoro-7-nitro-2,1,3-benzoxadiazole obtained by hard $\pi/2$ pulses from the thermal state, respectively, where the black curves indicate the spectra obtained in experiment and the red by simulation. We shifted the spectra by simulation for easier comparison with the spectra in experiment.

are listed in tables shown in Fig. 1. We illustrate the spectra obtained from the thermal states in Figs. 2 and 3. In molecule (a), we assign the spins F, H1 and H2 as qubits 1–3. The Hamiltonian of this system corresponds to Eq. (1) if we neglect scalar couplings, which are significantly smaller than the dipolar couplings.

As a test of controllability in the three-qubit system, we performed a numerical search of shaped pulse for implementing specific gates. The gate operations chosen for

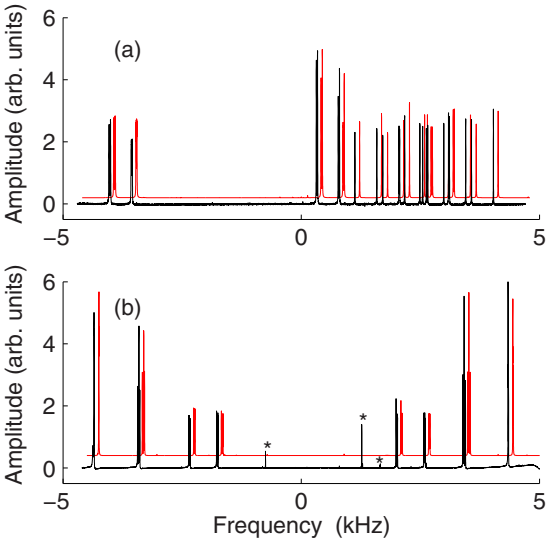

FIG. 3. (Color online) (a) ^{19}F and (b) ^{1}H -NMR spectra of 1,2-difluoro-4-iodobenzen obtained by hard $\pi/2$ pulses from the thermal state respectively, where the black curves indicate the spectra obtained in experiment and the red by simulation. (b) Peaks indicated with an asterisk come from the acetone in the coaxis capillary that is used for locking the field.

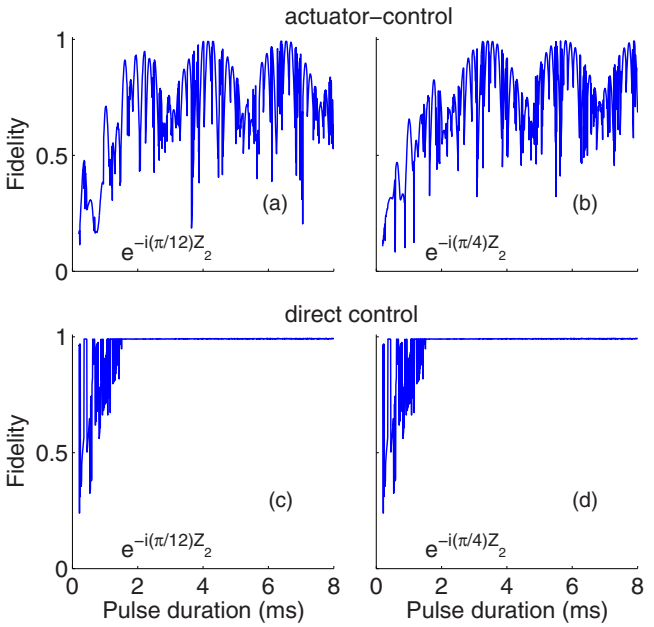

FIG. 4. (Color online) Fidelities reached in simulated optimized gate operations as a function of the pulse duration for $U_{z,2}(\theta) = e^{i\theta Z_2/2}$, with $\theta = -\pi/6$ and $-\pi/2$. Fidelities above 0.99 are reached for specific pulse durations. The panels in the bottom part of the figure show the corresponding fidelities for the case of full control of all qubits.

this test were single-qubit rotations $U_{z,2}(\theta)$, as defined by Eq. (12) of qubit 2 around the z axis, with rotation angles $\theta_1 = -\pi/6$ and $\theta_2 = -\pi/2$. We optimized the time-dependent amplitude and phase of the pulses, using a gradient ascent pulse engineering (GRAPE) algorithm [29,30], and obtained high fidelities (>0.99) with a control field amplitude of up to 12.5 kHz. Figures 4(a) and 4(b) show the fidelities that were obtained. In both cases, fidelities >0.99 were achieved for certain durations. For comparison, we also present the corresponding results with direct control, where the control pulses are applied to all qubits. These results are shown as Figs. 4(c) and 4(d).

One remarkable result of Figs. 4(a) and 4(b) is that high fidelity cannot be reached for all pulse durations, but only for some specific durations. This is an expected consequence of the discussion around Eq. (9) and holds not only for the specific rotation angles used in Fig. 4. Figure 5 illustrates this point by plotting the pulse durations required to obtain fidelities >0.99 for various rotation angles θ.

IV. EXPERIMENTAL RESULTS

A. Three-qubit system

As specific examples, we implemented the following operations in the three-qubit system:

$$U_{z,k}(-\pi/2) = e^{-i\frac{\pi}{4}Z_k}, \tag{14}$$

$$U_z(-\pi) = e^{-i\frac{\pi}{2}(Z_2+Z_3)}, \tag{15}$$

$$U_{23}(\theta) = e^{i\theta(X_2X_3+Y_2Y_3)}. \tag{16}$$

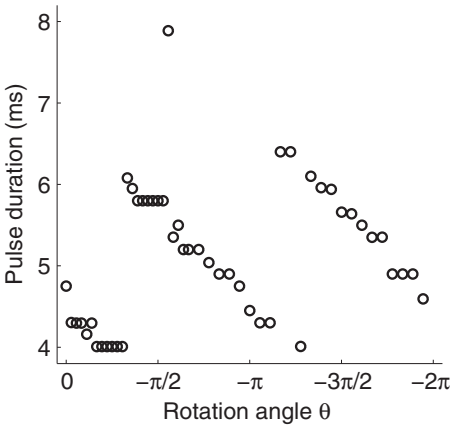

FIG. 5. Pulse duration changing with the rotation angle θ for implementing $U_{z,2}(\theta) = e^{i\theta Z_2/2}$ with the calculated fidelity higher than 0.99.

All three gates are important operations for quantum information processing. The gate in Eq. (16) can be used as a SWAP gate (up to a known phase factor) by choosing $\theta = \pi/4$, or as an entangling gate, with $\theta = \pi/8$.

The strong coupling between the homonuclear spins makes it difficult to excite only a single spin. Here we used the GRAPE algorithm to generate the control pulses. The calculated fidelities of the operations are >0.99. Table I summarizes the pulse durations and the simulated fidelities for these pulses.

The single-qubit gates should generate the transformations $U_{z,a}(-\pi/2) : X_a \to Y_a \to -X_a$, where $U : \rho_A \to \rho_B$ denotes $U\rho_A U^\dagger = \rho_B$. The two-qubit gate $U_{ab}(\pi/4)$ is equivalent to the SWAP gate, up to a phase gate, and can be represented as

$$U_{ab}(\pi/4) = \begin{pmatrix} 1 & 0 & 0 & 0 \\ 0 & 0 & i & 0 \\ 0 & i & 0 & 0 \\ 0 & 0 & 0 & 1 \end{pmatrix}. \tag{17}$$

TABLE I. Parameters of the pulses for implementing the quantum gates. The maximum control field amplitudes are 12.5 and 20 kHz in the three- and five-qubit systems, respectively.

Gate	Function	Pulse duration (ms)	Calculated fidelity
$U_z(-\pi)$	z rotation for qubits 2 and 3 in 3 qubits	2.36	>0.99
$U_{z,2}(-\frac{\pi}{2})$	z rotation for qubit 2 in 3 qubits	5.8	>0.99
$U_{z,3}(-\frac{\pi}{2})$	z rotation for qubit 3 in 3 qubits	5.8	>0.99
$U_{23}(\theta)$	XY interaction in 3 qubits	7	>0.99
$U_{45}(\pi/4)$	XY interaction in 5 qubits	14.2	>0.987

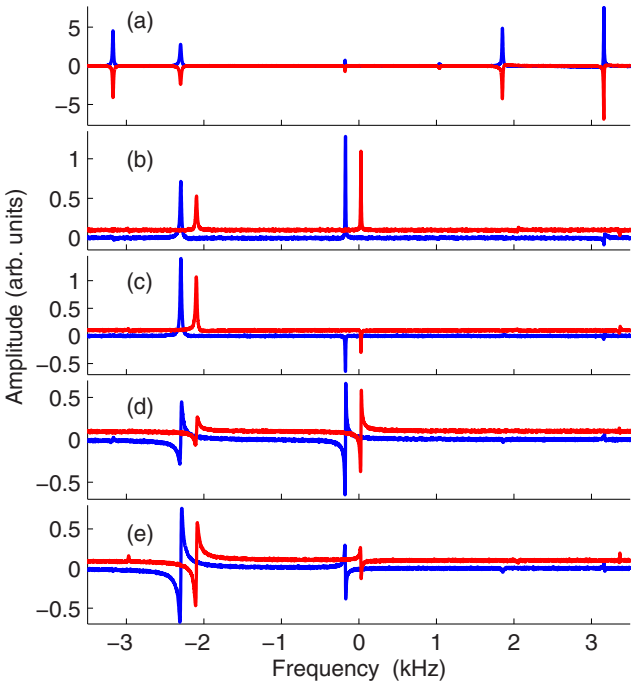

FIG. 6. (Color online) Experimental ^{1}H-NMR spectra of 4-fluoro-7-nitro-2,1,3-benzoxadiazole demonstrating the implementation of quantum gates. The blue curves in (a)–(e) show reference spectra for the states $EYE + EEY$, $\mathbf{10}X$, $\mathbf{1}X\mathbf{0}$, $\mathbf{10}Y$, and $\mathbf{1}Y\mathbf{0}$, respectively. The red curves show the results of the implementation of the gates $U_z(-\pi)$ to $EYE + EEY$, $U_{z,3}(-\pi/2)$ to $-\mathbf{10}Y$, $U_{23}(\pi/4)$ to $-\mathbf{10}Y$, $U_{23}(\pi/4)$ to $\mathbf{1}X\mathbf{0}$, and $U_{z,2}(-\pi/2)$ to $\mathbf{1}X\mathbf{0}$. In (b)–(e) we shifted the red spectra for easier comparison with the reference spectra.

1. Implementation of $U_z(-\pi)$

To demonstrate the operation $U_z(-\pi)$ defined in Eq. (15), we applied it to the input state $EYE + EEY$, where we use the abbreviated notation $ABC = A_1 \otimes B_2 \otimes C_3$. Following the usual convention for ensemble quantum computing, we describe the system by its deviation density matrix, i.e., the traceless part of the density operator [31]. The input state thus corresponds to the target qubits oriented along the y axis, and the z rotation should rotate them to the $-y$ axis.

Figure 6(a) shows the experimental result. The spectra were obtained by letting the two states before and after applying the gate operation evolve under the drift Hamiltonian, measuring the y magnetization of the system as a function of time and applying a Fourier transformation. Comparing the two spectra, we find the expected effect that the $U_z(-\pi)$ operation inverts the transverse spin components and thus the observable resonance lines. The absolute value of the spectral lines after the inversion is reduced by $\approx 14\%$, to $c = -0.86 \pm 0.09$. This reduction can be attributed to relaxation: the transverse relaxation times for H1 and H2 range from 14 to 36 ms, as determined from the width of the resonance lines.

2. Implementation of $U_{z,k}(-\pi/2)$ and $U_{23}(\pi/4)$

For implementing the gates $U_{z,k}(-\pi/2)$, and $U_{23}(\theta)$, we chose elements from the set

$$\{\mathbf{10}X, -\mathbf{10}Y, \mathbf{1}X\mathbf{0}, -\mathbf{1}Y\mathbf{0}\} \tag{18}$$

TABLE II. Measured overlaps obtained by fitting the spectra. The input states are listed in the first column and the gate operations in the first row. The state of the actuator qubit(s) is omitted. The values in columns 1–3 were obtained with the three-qubit system, and the last column with the five-qubit system.

	$R_{z,a}(-\pi/2)$	$R_{z,b}(-\pi/2)$	$U_{ab}(\pi/4)$ (3 qubits)	$U_{ab}(\pi/4)$ (5 qubits)
$\mathbf{0}_a X_b$	–	0.69 ± 0.04	0.67 ± 0.02	0.59 ± 0.04
$-\mathbf{0}_a Y_b$	–	0.68 ± 0.04	0.68 ± 0.02	0.60 ± 0.03
$X_a \mathbf{0}_b$	0.70 ± 0.02	–	0.58 ± 0.04	0.64 ± 0.09
$-Y_a \mathbf{0}_b$	0.71 ± 0.02	–	0.58 ± 0.04	0.68 ± 0.04

as input states, where $\mathbf{0} \equiv |0\rangle\langle 0|$ and $\mathbf{1} \equiv |1\rangle\langle 1|$. The states were chosen to give readily observable signals in NMR spectra as shown in Figs. 6(b)–6(e). They constitute a basis for the gates i.e., the set is closed under the effect of the gates. We prepared these input states using the established techniques [28,32]. The duration of the pulse sequence for preparing each input state was 4 ms.

Figures 6(b)–6(e) show the experimental results. To quantify the performance of the gates, we independently prepared the predicted final states $\mathbf{10}X, \mathbf{1}X\mathbf{0}$, $\mathbf{10}Y$, and $\mathbf{1}Y\mathbf{0}$ and measured their spectra. These reference spectra are shown as the blue curves. The red curves represent the results of the operations. They are shown next to the reference spectrum for the expected final state for ready comparison. The relative amplitudes of the two spectra in each figure yields the overlap of the state after the gate implementation with the predicted final state. Table II lists the measured overlaps. The reduction of the overlap, compared to the ideal value of 1, is mostly due to the decoherence accumulated during the gate operation.

3. *Implementation of $U_{23}(\theta)$*

For an arbitrary angle θ, $U_{23}(\theta)$ transfers the input state to a linear combination of two states from set (18) as

$$\begin{aligned} U_{ab}(\theta) : X_a \mathbf{0}_b &\rightarrow X_a \mathbf{0}_b \cos(2\theta) + \mathbf{0}_a Y_b \sin(2\theta), \\ Y_a \mathbf{0}_b &\rightarrow Y_a \mathbf{0}_b \cos(2\theta) - \mathbf{0}_a X_b \sin(2\theta). \end{aligned} \tag{19}$$

For the experimental data, we determined the corresponding coefficients by fitting the measured spectra to a linear combination of the corresponding reference spectra, which are shown as the blue curves in Figs. 6(b)–6(e). Figure 7 shows the resulting overlap coefficients when $U_{23}(\theta)$ was applied to the four input states. As a function of the rotation angle θ, the individual data points can be fitted to $A\cos(2\theta)$ and $B\sin(2\theta)$. By fitting the data in Fig. 7, we obtain A and B for the different input states. The results are listed in Table III.

B. Five-qubit system

In the five-qubit system, we implemented $U_{45}(\pi/4)$ on the target qubits. The control pulse was generated by the GRAPE algorithm with a theoretical fidelity > 0.987, with

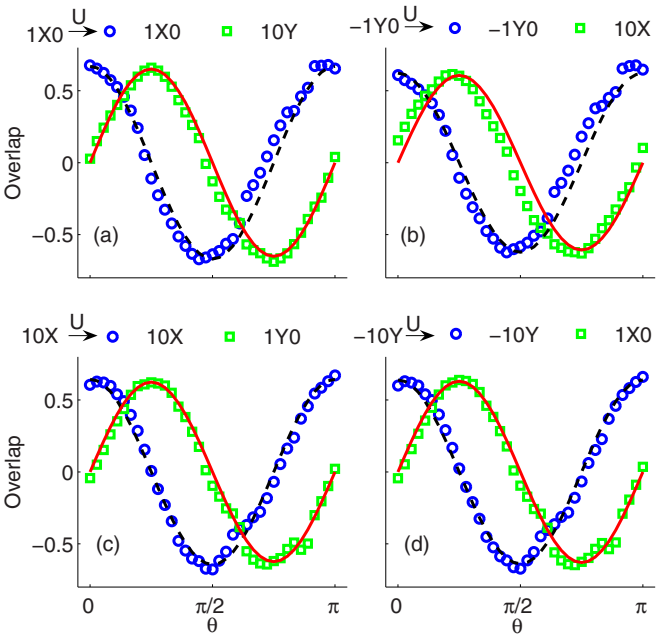

FIG. 7. (Color online) Experimental results of implementing $U_{23}(\theta)$ in the three-qubit system for the input states $\mathbf{1}X\mathbf{0}, -\mathbf{1}Y\mathbf{0}, \mathbf{10}X$, $-\mathbf{10}Y$, shown as panels (a)–(d), respectively. The basis operators for which the overlaps are determined are given in each panel. The solid and dashed curves are fits to the experimental data points.

the contributions of the scalar couplings included. In Table I, we summarize the parameters of the pulse.

For implementing $U_{45}(\pi/4)$ in the five-qubit system, we chose the input states as

$$\{\mathbf{0000}X, -\mathbf{0000}Y, \mathbf{000}X\mathbf{0}, -\mathbf{000}Y\mathbf{0}\}. \tag{20}$$

The pulse duration was 20 ms.

Figure 8 shows the experimental results. As in the case of the three-qubit system, we show the experimental results after the gate operation as the red curves next to the reference spectra (blue curves) for the expected target state. The measured spectra have the expected shapes but a reduced amplitude mainly resulting from decoherence. The last column in Table II quantifies this reduction, which is comparable to the values obtained in the three-qubit system.

TABLE III. The amplitudes for the oscillations of the overlap coefficients in Fig. 7. The input states are listed in the first column. The amplitudes A and B are obtained through fitting the data marked by circles and squares using functions $A\cos(2\theta)$ and $B\sin(2\theta)$, respectively.

	A	B
$\mathbf{1}X\mathbf{0}$	0.669 ± 0.021	0.651 ± 0.008
$-\mathbf{1}Y\mathbf{0}$	0.622 ± 0.026	0.607 ± 0.035
$\mathbf{10}X$	0.644 ± 0.008	0.624 ± 0.007
$-\mathbf{10}Y$	0.639 ± 0.007	0.630 ± 0.007

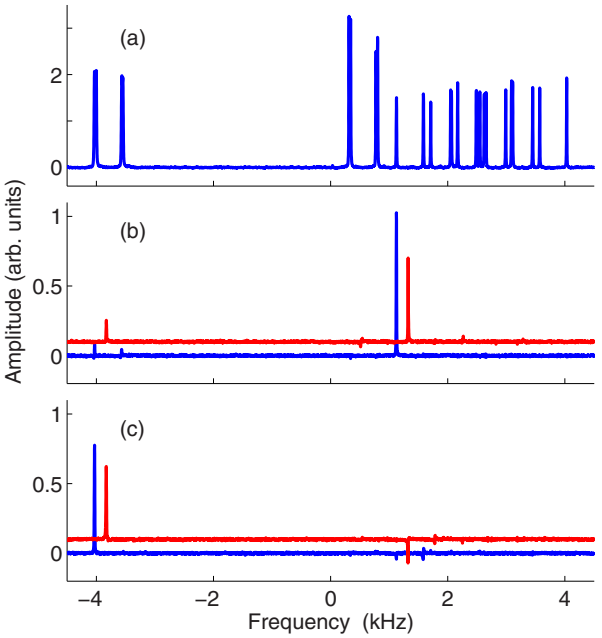

FIG. 8. (Color online) Experimental ^{19}F-NMR spectra of 1,2-difluoro-4-iodobenzene, demonstrating the performance of operation $U_{45}(\pi/4)$ in the five-qubit system. The spectra represented as the blue curves in panels (a)–(c) are obtained from the states $EEEXE + EEEEX, \mathbf{000}X\mathbf{0}$, and $\mathbf{0000}X$, respectively. The spectra represented as the red curves in panels (b)–(c) result from the implementation of $U_{45}(\pi/4)$ to $-\mathbf{0000}Y$ and $-\mathbf{000}Y\mathbf{0}$.

V. FIDELITY AND DECOHERENCE

The main contributions to the imperfections of the gate implementation can be attributed to (i) finite precision of the calculated control operations, (ii) relaxation, and (iii) experimental errors in the implementation of the gate. For the the single-qubit gates $U_{z,k}(-\pi/2)$ in the three-qubit system, we exploited quantum process tomography [5,33] to quantitatively evaluate the experimental performance. The χ matrix is exploited to completely characterize the process, and it can map an arbitrary input state ρ_{in} into the output state as

$$\rho_{\text{out}} = \sum_{ml} \chi_{ml} e_m \rho_{\text{in}} e_l^{\dagger}, \tag{21}$$

where the operators $e_{m,l} \in \{E, X, -iY, Z\}$ denote the basis set for describing the process, and the indices $m,l = 1, ..., 4$ run over the elements of the basis set. The measurement of χ requires the preparation of four input states $\rho_{\text{in}} = E, X, Y$, and Z. Here we have omitted the indices of the operators, because we consider only single-qubit operations. Quantum state tomography was used to determine the output state ρ_{out} for each ρ_{in}. Since the unit operator E is always time independent, the corresponding input state is omitted, assuming the output state is E. Figure 9 shows the χ matrices for the ideal and experimental gate operations.

For each process, we quantified the performance by comparing the experimental (χ_{exp}) and theoretical expectation (χ_{th}) χ matrices via the fidelity [34–36]

$$F_{\chi} = |\text{Tr}(\chi_{\text{exp}} \chi_{\text{th}}^{\dagger})| / \sqrt{\text{Tr}(\chi_{\text{exp}} \chi_{\text{exp}}^{\dagger}) \text{Tr}(\chi_{\text{th}} \chi_{\text{th}}^{\dagger})}. \tag{22}$$

The measured fidelities for $U_{z,2}(-\pi/2)$ and $U_{z,3}(-\pi/2)$ are 0.957 and 0.952, respectively.

In the five-qubit system, we used numerical simulations of the experiment to quantify the contributions (i)–(iii) and estimated that the fidelity loss for the gate $U_{45}(\pi/4)$ resulting from (i)–(iii) is 4%, 26%, and 8%, respectively.

Our experimental setup allows direct control of all qubits. As discussed in Sec. III, applying direct control operations can reduce the durations of the gate operations. As an example,

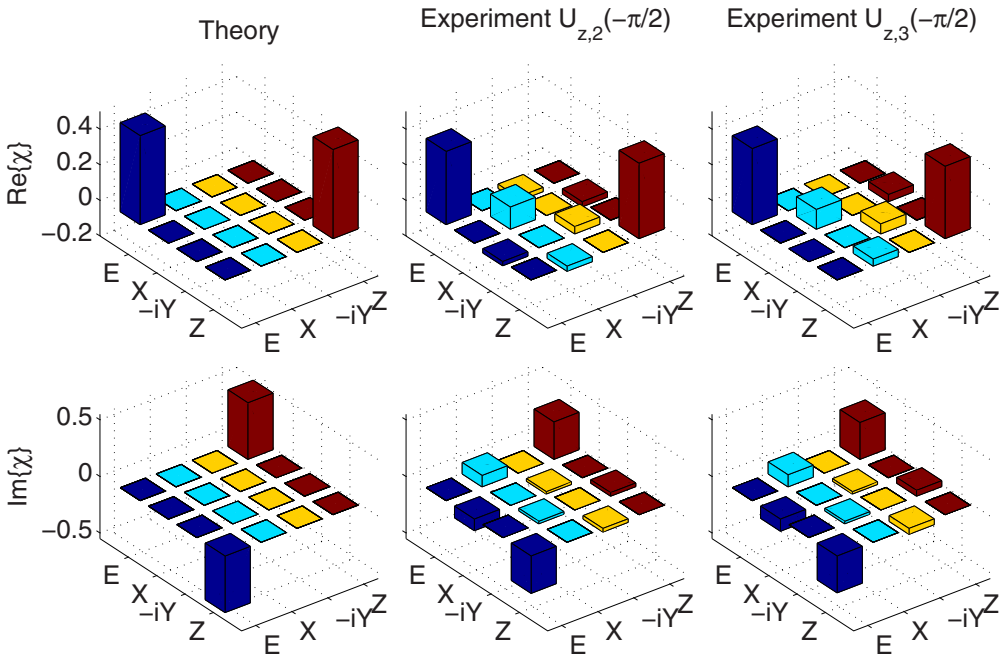

FIG. 9. (Color online) χ matrices obtained by quantum process tomography for $e^{-i\pi Z/4}$ for the ideal gate and for the experimental implementations on qubits 2 and 3.

we compare the required pulse durations in the actuator- and direct-control protocols for generating $U_{z,2}(-\pi/6)$ and $U_{z,2}(-\pi/2)$, using the results by numerical simulation presented in Fig. 4. Achieving fidelities > 0.99 in the actuator protocol requires minimal durations of 4.0 and 3.26 ms, while in the direct control protocol 1.52 ms is sufficient. Nevertheless, the actuator-control protocol is useful in certain cases, because it reduces the requirements for hardware resources, which may be a critical factor for implementing complex quantum algorithms, such as magic state distillation [37] and quantum error correction [38]. Furthermore, it can be significantly faster if the Rabi frequency for the direct-control is smaller than that of the actuator qubits.

VI. CONCLUSION

The purpose of this paper was the demonstration that a suitable combination of local control operations to a subsystem of the total quantum system, together with a suitable drift Hamiltonian, allows control not only over the directly controlled qubits (the actuator qubits), but also partial or full control of the target qubits. For this demonstration, we used two types of nuclear spins, with one type representing the actuator qubits, the other the target qubits. The couplings between the qubits were magnetic-dipole interactions. The results show good agreement between theory and experiment. While these results were obtained with nuclear spins, the same concept should be applicable to other systems, such as nitrogen-vacancy centers in diamond [39,40], where the hyperfine interactions provide sufficient resources.

ACKNOWLEDGMENTS

J.Z. acknowledges helpful discussions with J. Filgueiras, and experimental assistance from M. Holbach and J. Lambert. This work is supported by the DFG through Su 192/19-1 and by the DAAD. R.L. thanks CIFAR and Industry Canada for support.

[1] P. Kràl, I. Thanopulos, and M. Shapiro, Rev. Mod. Phys. **79**, 53 (2007).
[2] L. M. K. Vandersypen and I. L. Chuang, Rev. Mod. Phys. **76**, 1037 (2005).
[3] T. D. Ladd, F. Jelezko, R. Laflamme, Y. Nakamura, C. Monroe, and J. L. O'Brien, Nature (London) **464**, 45 (2010).
[4] C. H. Bennett and D. P. DiVincenzo, Nature (London) **404**, 247 (2000).
[5] M. A. Nielsen and I. L. Chuang, *Quantum Computation and Quantum Information* (Cambridge University Press, Cambridge, 2000).
[6] J. Stolze and D. Suter, *Quantum Computing: A Short Course from Theory to Experiment*, 2nd ed. (Wiley-VCH, Berlin, 2008).
[7] P. Zanardi and M. Rasetti, Phys. Rev. Lett. **79**, 3306 (1997).
[8] J. Wrachtrup and F. Jelezko, J. Phys. Condens. Matter **18**, S807 (2006).
[9] J. J. L. Morton, A. M. Tyryshkin, R. M. Brown, S. Shankar, B. W. Lovett, A. Ardavan, T. Schenkel, E. E. Haller, J. W. Ager, and S. A. Lyon, Nature (London) **455**, 1085 (2008).
[10] M. W. Doherty, N. B. Manson, P. Delaney, F. Jelezko, J. Wrachtrup, and L. C. Hollenberg, Phys. Rep. **528**, 1 (2013).
[11] T. W. Borneman, C. E. Granade, and D. G. Cory, Phys. Rev. Lett. **108**, 140502 (2012).
[12] D. Burgarth, K. Maruyama, M. Murphy, S. Montangero, T. Calarco, F. Nori, and M. B. Plenio, Phys. Rev. A **81**, 040303 (2010).
[13] R. Heule, C. Bruder, D. Burgarth, and V. M. Stojanovic, Phys. Rev. A **82**, 052333 (2010).
[14] N. Khaneja, Phys. Rev. A **76**, 032326 (2007).
[15] J. S. Hodges, J. C. Yang, C. Ramanathan, and D. G. Cory, Phys. Rev. A **78**, 010303 (2008).
[16] Y. Zhang, C. A. Ryan, R. Laflamme, and J. Baugh, Phys. Rev. Lett. **107**, 170503 (2011).
[17] D. D'Alessandro, *Introduction to Quantum Control and Dynamics* (Taylor and Francis, Boca Raton, FL, 2008).
[18] I. Dzyaloshinsky, J. Phys. Chem. Solids **4**, 241 (1958).
[19] T. Moriya, Phys. Rev. **120**, 91 (1960).
[20] C. H. Tseng, S. Somaroo, Y. Sharf, E. Knill, R. Laflamme, T. F. Havel, and D. G. Cory, Phys. Rev. A **61**, 012302 (1999).
[21] N. Khaneja, S. J. Glaser, and R. Brockett, Phys. Rev. A **65**, 032301 (2002).
[22] H. Yuan, D. Wei, Y. Zhang, S. Glaser, and N. Khaneja, Phys. Rev. A **89**, 042315 (2014).
[23] M. Christandl, N. Datta, A. Ekert, and A. J. Landahl, Phys. Rev. Lett. **92**, 187902 (2004).
[24] J. Zhang, G. L. Long, W. Zhang, Z. Deng, W. Liu, and Z. Lu, Phys. Rev. A **72**, 012331 (2005).
[25] J. Zhang, N. Rajendran, X. Peng, and D. Suter, Phys. Rev. A **76**, 012317 (2007).
[26] R. Laflamme, C. Miquel, J. P. Paz, and W. H. Zurek, Phys. Rev. Lett. **77**, 198 (1996).
[27] E. Knill, R. Laflamme, R. Martinez, and C. Negrevergne, Phys. Rev. Lett. **86**, 5811 (2001).
[28] J. Zhang, R. Laflamme, and D. Suter, Phys. Rev. Lett. **109**, 100503 (2012).
[29] N. Khaneja, T. Reiss, C. Kehlet, T. Schulte-Herbruggen, and S. J. Glaser, J. Magn. Reson. **172**, 296 (2005).
[30] C. A. Ryan, C. Negrevergne, M. Laforest, E. Knill, and R. Laflamme, Phys. Rev. A **78**, 012328 (2008).
[31] I. L. Chuang, N. Gershenfeld, M. G. Kubinec, and D. W. Leung, Proc. R. Soc. London A **454**, 447 (1998).
[32] E. Knill, R. Laflamme, R. Martinez, and C.-H. Tseng, Nature (London) **404**, 368 (2000).
[33] I. L. Chuang and M. A. Nielsen, J. Mod. Opt. **44**, 2455 (1997); J. F. Poyatos, J. I. Cirac, and P. Zoller, Phys. Rev. Lett. **78**, 390 (1997).
[34] X. Wang, C.-S. Yu, and X. X. Yi, Phys. Lett. A **373**, 58 (2008).
[35] A. M. Souza, G. A. Álvarez, and D. Suter, Phys. Rev. A **86**, 050301 (2012).
[36] J. Zhang, A. M. Souza, F. D. Brandao, and D. Suter, Phys. Rev. Lett. **112**, 050502 (2014).
[37] A. M. Souza, J. Zhang, C. A. Ryan, and R. Laflamme, Nat. Commun. **2**, 169 (2011).
[38] J. Zhang, M. Grassl, B. Zeng, and R. Laflamme, Phys. Rev. A **85**, 062312 (2012).
[39] J. H. N. Loubser and J. A. van Wyk, Rep. Prog. Phys. **41**, 1201 (1978).
[40] B. Smeltzer, L. Childress, and A. Gali, New J. Phys. **13**, 025021 (2011).